Geometric and Electronic Structure of the Aqueous $Al(H_2O)_6^{3+}$ Complex

Michael B. Hay*,† and Satish C. B. Myneni‡,§

Department of Civil and Environmental Engineering, Princeton University, Princeton, New Jersey 08544, Department of Geosciences, 151 Guyot Hall, Princeton University, Princeton, New Jersey 08544, and Earth Sciences Division, Lawrence Berkeley National Laboratory, Berkeley, California 94720

Received: March 27, 2008; Revised Manuscript Received: July 25, 2008

The bonding environment of the aqueous $Al(H_2O)_6^{3+}$ complex was studied using X-ray absorption near-edge structure (XANES) spectroscopy at the Al K-edge, with spectral interpretations based on density functional theory (DFT). Calculations for a highly symmetric complex (T_h symmetry) indicate electron transitions into Al 3p−O 2s and Al 3 p−O 2p antibonding orbitals, with a split O 2p contribution that appears to be due to a weak π-interaction of the Al 3p orbitals with water ligands off-axis (equatorial) with respect to the Al 3p axis. Calculations were performed with several hypothetical structures to assess the effects of Al−O bond length, orientation of water ligands in the first coordination shell, and the presence of a second solvation shell on the XANES spectrum. Similar transitions were observed in all of these cases, but with further splitting on addition of 12 solvation waters, inward tilting and random twisting of the water ligands, and nonuniform Al−O bond lengths. Although it was previously hypothesized that the broadness of the XANES spectrum for this complex is due to an asymmetric geometry, these results illustrate how an $Al(H_2O)_6^{3+}$ geometry that is octahedral (O_h) with respect to the $Al-O_6$ core could produce the broad spectrum observed. Because geometric distortions would affect relative Al−O bond strengths, an understanding of the equilibrium $Al(H_2O)_6^{3+}$ geometry is prerequisite to a quantitative description of reaction chemistry, including acidity and ligand exchange.

Introduction

Aluminum (Al), despite its ubiquity in the environment, is not an essential element for any organism. In the dissolved form, it poses a toxicity risk to plants and fish.[1−4] It is also a well-established neurotoxin in humans, playing a direct role in dialysis encephalopathy,[5] and a suspected role in amyotrophic lateral sclerosis/parkinsonian dementia complex (ALS/PDC) of Guam[6,7] and potentially Alzheimer's disease.[8,9] Though the toxicity risks of Al are balanced by its limited bioavailability at neutral pH, acidic conditions leading to Al dissolution may exist in environments exposed to acid rain, under highly oxidizing conditions such as in mine tailings,[10] or in deforested areas with high nitrification rates.[11] Once released into solution, Al speciation is often difficult to predict. In its simplest form, dissolved Al may be present as one of the mixed aqua/hydroxo complexes. $Al(H_2O)_6^{3+}$ and $Al(OH)_4^-$ are the most soluble complexes, present at low and high pH, respectively. Complexation with organic molecules and inorganic ligands (e.g., F^-) and the formation of quasi-stable polymeric species retain Al in bioavailable forms, even on return to neutral pH. Speciation is a particularly important factor in toxicity, as some forms appear to be more toxic than others.[3,12,13]

A detailed understanding of the behavior of Al in the environment and in biological systems requires knowledge of the various Al species present under different conditions, as well as a detailed understanding of their molecular and electronic structures. This is particularly true for the $Al(H_2O)_6^{3+}$ complex, as it is the highly soluble precursor to many of the chemical forms mentioned above. The influence of hydration structure on the chemical behavior of this complex is well-recognized and has been the subject of numerous ab initio studies.[14−25] Experimentally, the 6-fold coordination of the complex has been confirmed using ^{17}O and ^{27}Al NMR methods,[26,27] and an average Al−O bond length of 1.90 Å in solution was obtained using X-ray diffraction.[28,29] However, experimental verification of the detailed coordination geometry and electronic structure of this complex is lacking.

X-ray absorption near-edge structure (XANES) spectroscopy at the Al K-edge can provide additional details on the bonding environment of Al complexes and has been used extensively to study Al coordination in minerals.[30−42] For solution-phase complexes, XANES spectroscopy has the potential to reveal important electronic structure details with fewer complications from single- and multiple-scattering features compared to solid XANES. To the authors' knowledge, however, only two other aqueous-phase Al XANES reports currently exist in the literature. These studies, published by Matsuo et al., present XANES spectra and discrete variational Xα (DV-Xα) calculations on the $Al(H_2O)_6^{3+}$ and $Al(EDTA)^-$ complexes.[43,44] On the basis of a comparison of experimental and calculated XANES spectra, the authors predicted the equilibrium configuration of the $Al(H_2O)_6^{3+}$ complex in solution to be highly asymmetric,[43,44] though ab initio geometry optimizations are more consistent with a symmetric equilibrium geometry.[16,23,24] This distinction is important, as an asymmetry in geometry would imply unequal Al−O bond strengths, which would impact the water exchange rate, acidity, and ultimately the reactivity of the complex.

In this study, we present aqueous Al XANES spectra for the $Al(H_2O)_6^{3+}$ complex, along with spectral interpretations based on density functional theory (DFT) calculations. Insights into the electronic structure of this complex are gained through comparisons of calculation results for a series of hypothetical $Al(H_2O)_6^{3+}$ geometries, which are based on the reported ab

* Corresponding author. E-mail: mbhay@usgs.gov.
† Department of Civil and Environmental Engineering, Princeton University.
‡ Department of Geosciences, Princeton University.
§ Lawrence Berkeley National Laboratory.

10.1021/jp802675v CCC: $40.75
Published on Web 10/01/2008

initio-optimized geometries and include the effects of water ligand orientation, bond length variation, and the presence of second-shell solvation waters. This analysis provides a modified, in-depth interpretation for the $Al(H_2O)_6^{3+}$ XANES spectrum and its structural implications.

Experimental Section

Materials and Sample Preparation. Hydrated Al chloride, nitrate, and sulfate salts were purchased from Sigma-Aldrich. Aqueous Al samples were prepared using deionized water (Milli-Q, 18 MΩ resistivity) and were stored in acid washed plastic vials to avoid silicate contamination from glass. Aluminum solutions for spectroscopy were prepared through dilution of 100 mM stock solutions. Acid addition was performed using a stock HCl solution to yield the final desired Al concentration and pH (pH 0.4−3.6). X-ray analyses were typically performed between 1 and 24 h after sample preparation. pH values were measured between 0.4 and 3.6 using an Orion model 525A pH meter with Orion PerpHecT ROSS Model 8203 and Orion 9107BN pH electrodes.

X-ray Absorption Spectroscopy. Al K-edge XANES spectra were collected on the Molecular Environmental Sciences (MES) beamline 11.0.2 at the Advanced Light Source, Lawrence Berkeley National Laboratory (Berkeley, CA). Bulk aqueous-phase spectra were collected in fluorescence mode in a 1 atm He environment in the modified Soft X-ray Endstation for Environmental Research (SXEER-2).[45] Samples were held either in an open-faced soda straw, which permitted spectral collection at the air−water interface, or in a liquid sample cell fitted with a 100 nm thick Si_3N_4 window. A GaAsP photodiode and a photomultiplier tube (PMT), both obtained from Hamamatsu Corporation, were alternately used for fluorescence detection. The PMT was outfitted with a phosphor scintillator for detection of X-ray photons.

Spectra were collected from 1550 to 1600 eV, with step sizes of 0.2 eV in the edge region (1560−1573 eV or greater) and 0.5 eV below and above the edge. Baseline correction and postedge normalization were performed simultaneously by fitting straight lines to the spectra below and above the edge, then rescaling the spectra such that the slopes of the lines were zero and the pre and postedge line intercepts were 0 and 1, respectively. For energy calibration, a spectrum was collected in fluorescence mode on the polished surface of a single-crystal corundum sample (α-Al_2O_3, Union Carbide Crystal Products). The crystal surface was oriented normal to the incident beam, with the detector placed at a 90° angle from the incident beam (i.e., grazing, near-parallel view of the crystal surface) to minimize self-absorption effects in the fluorescence spectrum. Energy calibration involved shifting the first XANES peak in the corundum spectrum to 1567.5 eV.[42] Normalization, energy calibration, and spectral subtractions were performed using WinXAS[46] and Microsoft Excel.

Calculation of X-ray Absorption Spectra. X-ray absorption spectra were calculated using the Stockholm-Berlin ("StoBe-deMon," or "StoBe") software package,[47] a DFT based program, using the gradient corrected exchange functional of Becke[48] and correlation functional of Perdew[49] (see also Triguero et al.[50] for more theoretical details). Two effects in particular must be accounted for when calculating X-ray spectra: energy level shift upon removal of an electron from the 1s orbital (relaxation energy) and the probability of transition between a given pair of orbitals (oscillator strength). The relaxation energy is dealt with in StoBe using the Slater transition-state method,[51] which involves explicitly defining a half-electron occupation in the α-1s orbital. Oscillator strengths are calculated using the transition-potential approach.[50] To accurately model the postedge continuum-state transitions, StoBe employs a double-basis set technique, which involves inclusion of an additional set of diffuse basis functions (e.g., refs 52 and 53).

The calculated transition energies and oscillator strengths can be convoluted with Gaussians to produce a synthetic X-ray spectrum. In the default StoBe routine, the peak areas of the Gaussians are fixed by the oscillator strengths, and the peak widths are freely adjusted. In this work, the widths were adjusted in attempts to reproduce experimental spectra. To minimize the number of free parameters, only two peak width and two energy values are specified. Below the first energy value (E_1), a constant, relatively narrow width (w_1) is used. E_1 is typically chosen such that w_1 is used in the first part of the near-edge region. The second peak width value (w_2) is used above the second energy value (E_2). A broad value is chosen for w_2 such that the discrete post edge transitions yield a smooth profile past the edge. Between E_1 and E_2, the peak width varies linearly between w_1 and w_2 values, making the peak width continuous as a function of energy. For each transition, the StoBe program also outputs spatially resolved information on the molecular orbital densities, which are viewed using the program Molden.[54] The electron density images can be used to gain a qualitative picture of the types of atomic orbitals involved in bonding but do not yield quantitative information on the relative proportions of atomic orbitals involved in a particular bond.

The ionization potential was recalculated as the difference in total energy between the ground-state and fully ionized complex, i.e., between structures with Al α-1s orbital occupations of 1 and 0, respectively.[55] The energy scale for the calculated XANES transitions was recalibrated by shifting the ionization potential of the half-electron α-1s occupied complex to this new value. For the Al-edge calculations performed in this study, this shift varied between −2.49 and −2.85 eV. Aligning the spectra with experiment involved an additional shift of between −11.5 and +4.7 eV depending on the orbital basis sets used. The magnitude of these energy shifts is not critical in this study, however, because our analysis is focused on *relative* energy differences among transitions and how they change with geometry and basis set.

Most calculations were performed using the IGLO-III basis set on all elements.[56] This basis set is commonly used in X-ray absorption studies to account for core relaxation of the excited element (e.g., refs 52 and 57). For comparison with IGLO-III results, other basis sets available in the StoBe database (version 6) were also used. These included the DZVP, DZVP-2 (modified DZVP), and TZVP basis sets on O, H, and Al,[58] with field-induced polarization functions included in the TZVP basis set for O and H,[59] as well as the Lie and Clementi basis sets on O and H.[60] Using different basis sets on Al required different energy shifts to align the calculated and experimental results, with the IGLO-III Al basis set yielding results closest in energy to experiment. Due to a maximum limit on the number of orbital Gaussians allowed in the Windows version of StoBe, the $Al(H_2O)_6^{3+}$ calculation with explicit second-shell waters could not be run with the full IGLO-III basis set. For this calculation, IGLO-III was used on Al, and DZVP was used on O and H.

Results and Discussion

Aqueous Al XANES Spectra. It is well-established from NMR and X-ray diffraction measurements that the Al in the fully protonated aqua−Al complex is strongly bound to six water molecules in an octahedral geometry.[26−29] The XANES spectra

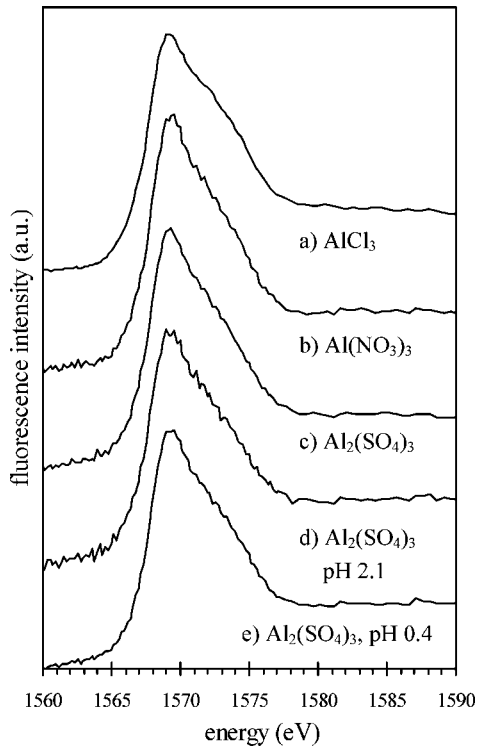

Figure 1. Al K-edge X-ray absorption spectra of 20 mM Al^{3+} salt solutions. Spectra a−c were collected on unacidified solutions (pH ~3.6), and spectra d and e were collected on solutions acidified with HCl. Spectra are the average of multiple scans, with the noisier spectra composed of fewer scans.

collected on aqueous Al solutions at and below pH 3.6 (Figure 1) are consistent with this proposed coordination number and geometry, based on comparison with XANES spectra of minerals containing Al in 6-coordination. Published XANES spectroscopic studies of numerous Al-oxides and clays, including corundum, diaspore, boehmite, kyanite, montmorillonite, kaolinite, and several others, place the first main 6-coordinate Al XANES feature between 1567.5 and 1569 eV (e.g., refs 30−42, see also references therein), whereas 4-coordinate Al (albite, natrolite, berlinite, sillimanite) yields a feature at lower energy near 1566 eV.[34,38] XANES spectra collected in our endstation on various mineral phases, including corundum, gibbsite, and andalusite, are consistent with these results. The first peak in the aqueous Al XANES spectrum occurs at 1569.2 eV. Although this value is slightly higher than the typical range observed for octahedral Al in the solid phase, it is considered to be consistent with 6-coordination.

XANES spectra a, b, and c in Figure 1 were collected on 20 mM $AlCl_3$, $Al(NO_3)_3$, and $Al_2(SO_4)_3$ salt solutions without pH adjustment. At 20 mM total Al, the $Al(H_2O)_6^{3+}$ complex buffers the pH to ~3.6 via deprotonation, while remaining the dominant species in solution. Speciation calculations performed using the stability constants of Martell and Smith[61] indicate that over 98% of the Al is in the form of $Al(H_2O)_6^{3+}$ for these solution conditions, with the remaining 1−2% present as the singly deprotonated species $AlOH^{2+}$ ($pK_{a1} = 5.0$) and various polymeric species.[45] The $Al(H_2O)_6^{3+}$ proportion becomes greater as the pH is lowered. To ensure that polymeric species had no effect on the $Al(H_2O)_6^{3+}$ XANES spectrum, data were also collected on solutions acidified with HCl to pH 2.1 and 0.4 (Figure 1, trace d and e, respectively). No significant differences are observed between spectra on acidified and nonacidified solutions. Further, because the solution spectra look identical for the three different counterions examined, it is clear that the counterion has no observable effect on the aqueous Al spectrum at these concentrations. To rule out Al concentration effects, spectra were also collected on more dilute solutions (data not shown). Acidified solutions as low as 5 mM, the lower limit imposed by detector sensitivity in our experiment, looked identical to the 20 mM spectra within the noise level. Though concentration and pH conditions were not specified in their study, our spectra are also consistent with the aqueous $Al(NO_3)_3$ spectrum reported by Matsuo et al.[43,44]

Calculated XANES Spectra. To understand the molecular orbitals involved in the aqueous Al XANES transitions, synthetic spectra were calculated for a number of idealized structures using the StoBe software package. Results are described in detail below, first for a highly symmetric structure, followed by structures that include varying Al−O bond lengths, reorientation (bending, twisting) of the first-shell water ligands, and addition of a second-shell solvation layer.

a. Highly Symmetric Structure. Baseline studies were performed on an idealized, highly symmetric $Al(H_2O)_6^{3+}$ structure with T_h point group symmetry (hereafter referred to as the T_h complex), shown in Figure 2A. The Al−O bond length of 1.90 Å was assigned on the basis of aqueous X-ray diffraction results.[28,29] The HOH bond length (0.99 Å) and bond angle (108°) were assigned on the basis of $Al(H_2O)_6^{3+}$ geometry optimization calculations and by analogy with $Cr(H_2O)_6^{3+}$ neutron diffraction results,[62] both summarized by Bylaska et al.[17] Typically, point group symmetry can be exploited in StoBe to decrease the time required for calculations, but the T_h point group was not available in StoBe. The calculations were therefore run using D_{2h} symmetry (a subgroup of the ideal T_h symmetry), which was available in StoBe.

To understand the XANES calculations, it is useful to investigate the ground-state structure of the complex. A summary of the occupied molecular orbitals and orbital energies calculated for the T_h complex is given in Table 1. A total of 35 filled orbitals (70 electrons) are present in the complex, with degenerate orbitals grouped into single lines in the table. Energies are listed for the nondegenerate orbitals of the ground-state, fully occupied Al 1s complex, calculated in StoBe using the IGLO-III basis set. These energies have been tabulated primarily for comparative purposes to illustrate the relative energy differences between orbitals. The apparent orbital contributions from Al and H_2O are also given, inferred on the basis of visual inspection of the electron density images obtained from Molden. The bonding orbitals of the complex are those that include both Al and H_2O contributions. A more complete table, including energies, symmetries, and electron isodensity surface plots for each occupied molecular orbital, is included in Table S1 in the Supporting Information.

The bonding molecular orbitals appear to come from Al 3s, 3p, and possibly 3d orbitals mixing primarily with filled water $2a_1$ and $3a_1$ orbitals. Electron isodensity surface plots are shown in Table 1 for the molecular orbitals with Al 3p contributions, with one of three degenerate orbitals shown for each set. Aluminum 3p contributions were inferred from the presence of the inner Al 3p lobes in the isodensity plots; these are largest and easiest to see in orbitals 25−27, suggesting that this set has the largest Al 3p contribution. Electron isodensity plots for all of the bonding orbitals, as well as a more complete description of how the orbital interactions were inferred from these plots, are given in Figure S1 (Supporting Information). Comparison of the isodensity plots for orbitals 19−21 with 25−27 (Table 1) illustrates a difference in phase of the Al 3p

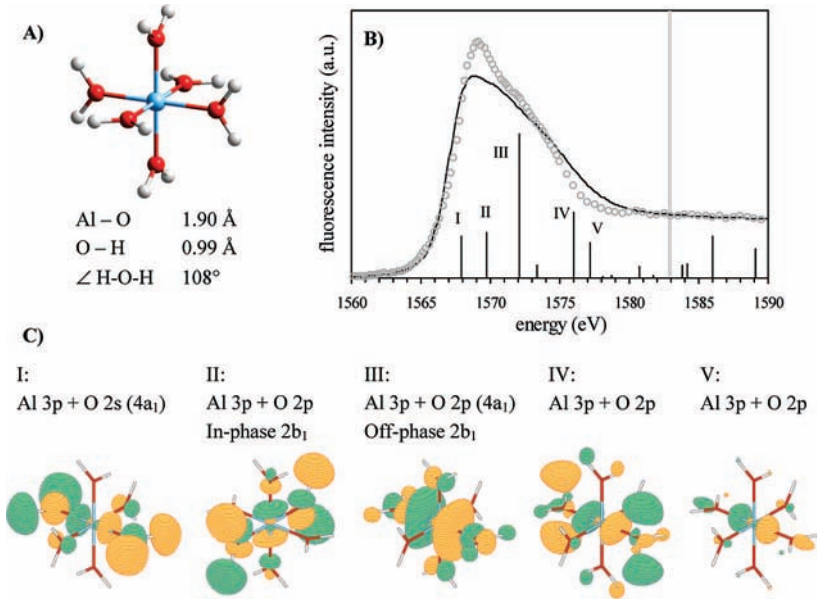

Figure 2. (A) Geometry of the highly symmetric $Al(H_2O)_6^{3+}$ complex with T_h point group symmetry. Blue = Al, red = O, and white = H. (B) XANES spectral transitions (thin vertical bars), ionization potential (gray vertical bar), and synthetic spectrum (solid curve) calculated for the structure in (A), plotted against the 20 mM aqueous $AlCl_3$ spectrum (circles). The calculated energies were shifted 4.7 eV to align them with the experimental spectrum. (C) Electron isodensity plots for the antibonding molecular orbitals corresponding to transitions I−V.

TABLE 1: Occupied Orbitals of the $Al(H_2O)_6^{3+}$ Complex with T_h Symmetry

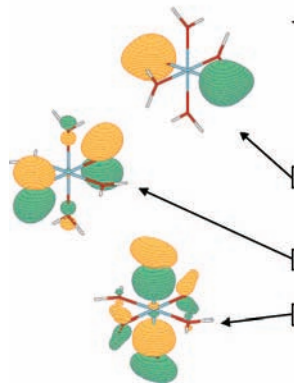

Orbital	E (eV)	Orbital contributions Al^{3+}	Orbital contributions H_2O
1	-1522.9	1s	
2-7	-525.9		$1a_1$
8	-122.0	2s	
9-11	-84.0	2p	
12	-40.7	3s	$2a_1$
13-15	-40.2	3p	$2a_1$
16,17	-40.0		$2a_1$
18	-28.3	3s	$3a_1$
19-21	-28.1	3p	$3a_1$, $1b_1$
22-24	-28.1		$1b_1$
25-27	-26.1	3p	$3a_1$, $1b_1$
28,29	-25.2	3d	$3a_1$
30-35	-22.4		$1b_2$

+ water $3a_1$ bonding orbitals with respect to the $1b_1$ orbitals on the waters perpendicular to the Al 3p axis (hereafter referred to as the "equatorial" water ligands). This difference in phase between Al 3p water $3a_1$ and water $1b_1$ orbitals is strong enough to cause the 2 eV energy difference between orbitals 19−21 and 25−27 (Table 1). Much of the electron density involved in Al binding could be expected to come from the nonbonding $1b_2$ electrons on water, but these orbitals are perpendicular to the Al−O axis, and hence cannot interact with Al in a σ fashion. It is possible that, although water orbitals are clearly recognizable, some rehybridization is occurring, moving electron density from the $1b_2$ into the $3a_1$ orbitals for bonding. Similar $1b_2/3a_1$ hybridization was experimentally observed for H-bonding in liquid water.[63]

The XANES calculation results for the T_h complex are shown in Figure 2B, including calculated electron transitions (represented by the thin vertical bars) and the synthetic XANES spectrum generated from the electron transitions, plotted against the experimental 20 mM $AlCl_3$ spectrum from Figure 1. The heights of the vertical bars represent the relative oscillator strength (probability) of each transition. The calculated transitions have been shifted by +4.7 eV to align the synthetic and experimental spectra. The calculation yields five sets of transitions in the near-edge region, represented by the bars labeled I−V in Figure 2B, where each bar is a set of three overlapping Al 1s transitions into degenerate antibonding orbitals. The synthetic spectrum shown represents the best attempt at reproducing the experimental spectrum by varying Gaussian peak widths, which required narrower Gaussians for transitions I and II than for IV and V. Disagreement between the theoretical and experimental spectra may largely be due to an underestimation of the oscillator strengths for transitions I and/or II relative to IV and V. The calculated ionization potential, represented by the thick gray line at 1584.1 eV in Figure 2B, occurs roughly 10 eV higher than expected, resulting from the unbalanced positive charge on the complex. As demonstrated below, this problem is alleviated when solvation waters or point charges are added in the calculation.

The antibonding orbitals corresponding to transition sets I−V are displayed in Figure 2C, labeled accordingly, with one of three antibonding orbitals shown for each transition set. These orbitals exhibit Al 3p−O 2s and Al 3p−O 2p antibonding interactions along the Al 3p axes. In the water molecule, both O 2s and O 2p contribute to the $4a_1$ antibonding orbital. Although some water $4a_1$ character is visible in the $Al(H_2O)_6^{3+}$ antibonding orbitals, particularly in orbitals I and III (Figure

2C), a description in terms of the O atomic orbitals is more useful in this context, because separate s and p contributions are observed.

The antibonding orbitals corresponding to transition set I, which occurs at 1567.9 eV after calibration (Figure 2B), include contributions from Al 3p and O 2s atomic orbitals (Figure 2C). These are most likely the antibonding counterparts of bonding orbitals 13−15 in Table 1. Antibonding orbitals for transitions II and III, located at 1569.7 and 1572.1 eV, respectively, both exhibit Al 3p and O 2p antibonding character along the Al 3p axes. Off-axis, however, orbital sets II and III exhibit Al 3p−O 2p (water $2b_1$) π interactions that differ in phase. In orbital II, the Al 3p and O 2p nodes are in-phase, whereas these nodes occur out of phase in orbital III. Orbitals II and III are the antibonding counterparts of the Al 3p bonding orbitals discussed above (19−21 and 25−27), consisting of Al 3p−water $3a_1$ σ bonds and Al 3p−$1b_1$ π interactions. Specifically, the antibonding set II orbitals are believed to correspond to bonding orbitals 19−21, and the antibonding set III orbitals are believed to correspond to bonding orbitals 25−27, on the basis of the relative sizes and shapes of the water orbitals (cf. Figure 2C, Table 1). Relative to 25−27, bonding set 19−21 has larger $1b_1$ orbital components and more atomic O 2p character over $3a_1$, similar to set II. This assignment is also consistent with the larger Al 3p density observed on bonding set 25−27 and antibonding set III.

Transitions IV and V also exhibit some Al 3p−O 2p character, though these are more difficult to interpret. Transition IV exhibits large clouds of delocalized electron density, but the electron density on the ligands is much weaker in transition V. It is possible that the StoBe calculation is overestimating the oscillator strengths for these sets of transitions, because they do not appear to be strong contributors in the experimental spectrum. The tenuous nature of these higher energy transitions is also suggested by a comparison of calculation results obtained using different basis sets, shown in Figure 3. In Figure 3a−c, alternate basis sets were used on all elements, and in Figure 3d−g, alternate basis sets were used on O and H only, as indicated in the figure. The results obtained with the full IGLO-III basis set are shown again in Figure 3h for comparison. Overall, the energies and oscillator strengths of transitions I−III exhibit little variation with basis set, with the exception of the Lie and Clementi basis set calculation, which yields a more intense, slightly lower energy Al 3p−O 2s transition (Figure 3d). In contrast, transitions IV and V are highly sensitive to the choice of basis set, particularly on O and H. For transition IV, this greater sensitivity to ligand basis set is consistent with the more diffuse nature of these orbitals (Figure 2). For these reasons, a greater emphasis is placed in this study on the first three sets of transitions.

b. Changes in Al−O Bond Length. Calculations were performed to assess the sensitivity of the X-ray spectrum to the $Al(H_2O)_6$ coordination geometry. In Figure 4a-c, the Al−O bond lengths were adjusted uniformly while retaining the T_h symmetry of the complex. When the Al−O bond length is shortened (Figure 4a), the oscillator strength of transitions I and II decrease relative to III, indicating a relative enhancement of the Al 3p + O 2p off-phase interaction discussed above. The energy difference between transitions II and III increases when the Al−O bond length is shortened, suggesting that the interaction of the Al with the off-axis waters becomes stronger as the waters are brought closer to the Al. The opposite effect is observed when the Al−O bond length is increased from 1.9 Å to 2.0 Å (Figure 4c); the energy difference between transitions II and III decreases, while the intensity of transitions I and II increase.

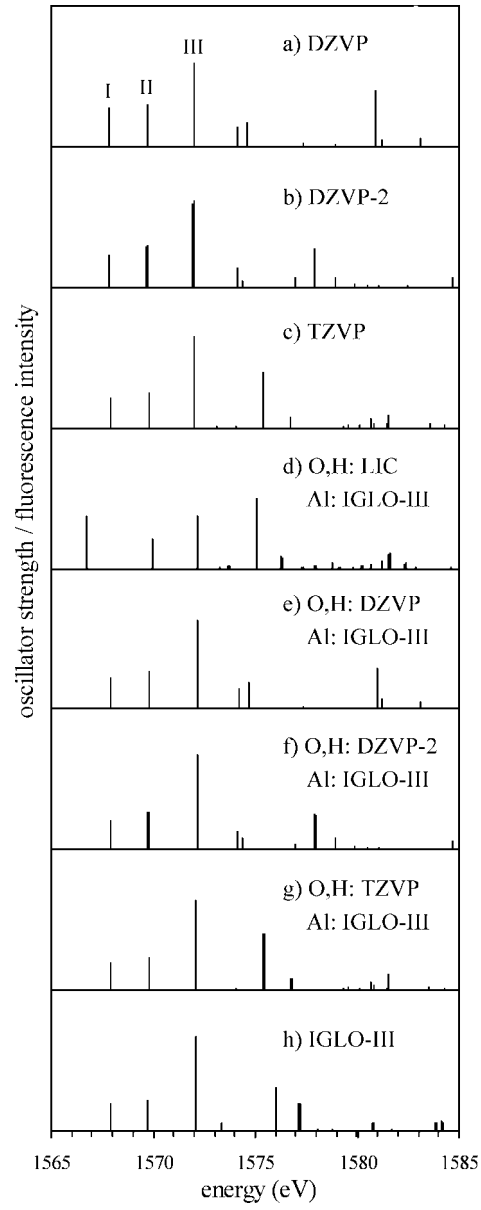

Figure 3. XANES transitions calculated for the highly symmetric (T_h) $Al(H_2O)_6^{3+}$ complex using different basis sets. The results from Figure 2 are replotted in (h) with the same 4.7 eV shift. Transitions in (a)−(g) were recalibrated to the same ionization potential as in (h), 1582.9 eV, for comparison.

As mentioned above, these transitions are each a set of three transitions corresponding to degenerate orbitals, and they remain degenerate when the Al−O bond lengths are varied uniformly. In Figure 4d, the structure was assigned nonuniform Al−O bond lengths, with four equatorial bonds of 1.85 Å and two axial bonds of 2.0 Å, yielding a structure with an average bond length of 1.9 Å. The structure no longer has T_h symmetry but retains D_{2h} symmetry. Although this type of distortion is common in other octahedral metal complexes, such as $Cr(H_2O)_6^{2+}$ and $Cu(H_2O)_6^{2+}$, the effect is most commonly due to incomplete d-orbital occupation (the Jahn−Teller effect).[64] Because this is not the case for Al, this choice of geometry in our study is essentially arbitrary. Regardless, the calculation demonstrates that bond length distortions in the complex can cause a splitting of the XANES transitions, particularly in transitions II and III.

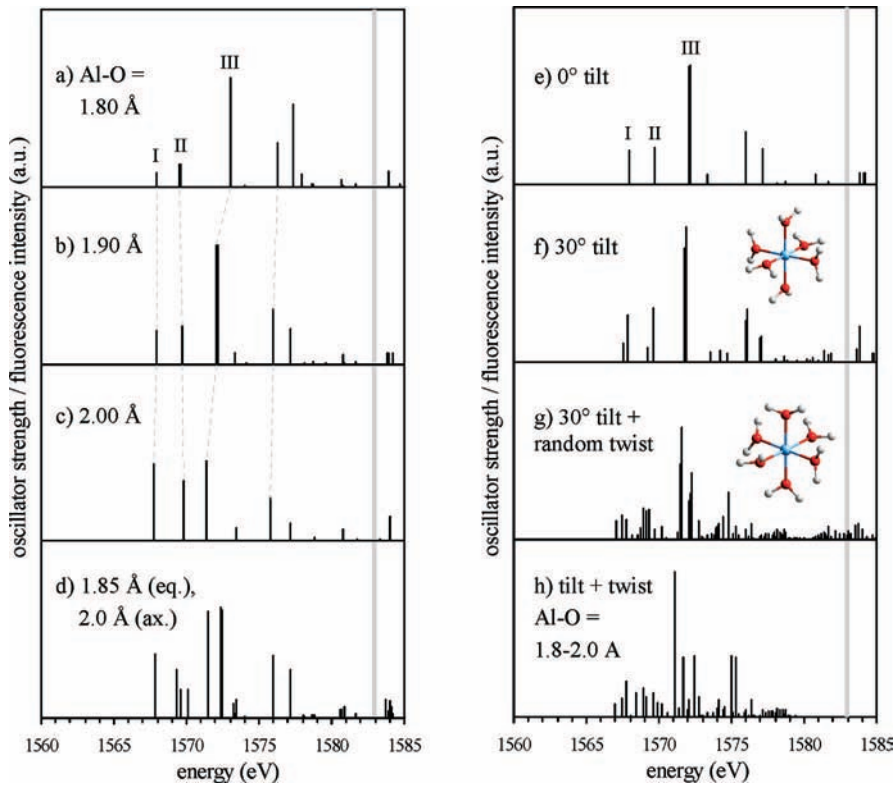

Figure 4. XANES transitions calculated for $Al(H_2O)_6^{3+}$ structures of varying geometry. In (a)−(d), the Al−O bond length is varied, retaining T_h symmetry in (a)−(c) and D_{2h} symmetry in (d). (a) Al−O length = 1.80 Å. (b) Al−O length = 1.90 Å (same structure as in Figure 2). (c) Al−O length = 2.00 Å. (d) Nonuniform Al−O bond lengths; four equatorial bonds of 1.85 Å and two axial bonds of 2.0 Å. In (e)−(h), water ligands are reoriented. (e) Same structure as Figure 2. (f) Water ligands tilted inward 30°. (g) Water ligands twisted randomly about the Al−O axis following 30° inward tilt as in (f). (h) Waters oriented as in (g), with nonuniform Al−O bond lengths distributed as in (d). Energies were recalibrated to an ionization potential of 1582.9 eV (gray vertical line).

The splitting observed in transition III is consistent with the changes in relative energies observed between structures of uniform bond length (Figure 4a−c), whereas the splitting of transition II would not have been predicted from the uniform bond length structures.

c. Changes in Water Orientation. In Figure 4e−h, the water ligand orientation was varied while retaining the octahedral symmetry of the $Al-O_6$ core. Figure 4f shows the spectrum for a structure in which the water ligands were tilted inward 30° but were not twisted along the Al−O bond relative to the original T_h structure, shown again in Figure 4e for comparison. The value of 30° was chosen on the basis of the theoretical results of Bylaska et al.,[17] who obtained average tilt values of between 25° and 30° in molecular dynamics simulations of the $Al(H_2O)_6^{3+}$ complex, in close agreement with the experimental $Cr(H_2O)_6^{3+}$ value of 34° obtained by neutron diffraction.[17,62] In the second structure (Figure 4g), the ligands were first tilted 30° and then twisted along their Al−O bonds by a random angle, on the basis of the assumption that this twist angle would be largely random in solution. The calculation in Figure 4f yields the same transitions found in the spectrum of the T_h complex, but some band splitting is observed, particularly in transitions I and II. This splitting of transitions I−III becomes more extreme when the waters are twisted about the Al−O axes (Figure 4g), and still more extreme when these water ligand orientations are assigned to a structure with nonuniform Al−O bond lengths (Figure 4h). Loss of orbital degeneracy causes the transitions to disperse along the energy axis, though distinct clusters are still observed corresponding to transitions I−III, and possibly IV at slightly lower energy than before (near 1575 eV).

d. Addition of Second-Shell Solvation Waters. Additional water molecules were added in the calculations to test the effect of solvation on the $Al(H_2O)_6^{3+}$ XANES spectrum. Twelve water molecules were uniformly positioned in the second shell to yield an $Al-O_{II}$ (Al to second-shell oxygen) distance of 4.01 Å and an O_I-O_{II} distance of 2.73 Å (see schematic, Figure 5). These distances correspond to the average values obtained in recent molecular dynamics (MD) simulations and aqueous XRD results on the $Al(H_2O)_6^{3+}$ complex.[17,29] The second shell waters were oriented such that they form H-bonds with the first-shell waters, thereby saturating the H-bond donor capacity of the first shell, consistent with ab initio geometry optimizations and MD simulations.[14,16−18,23,25] The structure retains T_h point group symmetry, with D_{2h} symmetry used in the calculations. The second-shell water molecules were added in two separate calculations: one in which the waters were represented as a series of point charges, and one in which they were represented as explicit molecules.

Solvation waters added as point charges were assigned charge magnitudes of −1.186 and +0.593 on each of the respective O and H atoms. These charge values are based on ab initio calculations of the electron "sharing index" and effectively represent the residual valence of the O and H atoms in the water molecule.[65] As point charges, the solvation waters exhibit an electrostatic influence on the $Al(H_2O)_6^{3+}$ complex only. The calculated XANES transitions, shown in Figure 5b, are similar to the results obtained for the original structure lacking solvation waters (shown again in Figure 5a) but exhibit two sets of transitions with Al 3p−O 2s character analogous to transition I, based on investigation of the molecular orbitals (Figure S2, Supporting Information). It is not entirely clear why two O 2s contributions appear with the addition of point charges. The antibonding orbitals for these transitions suggest that the difference may again be due to differences in electron density

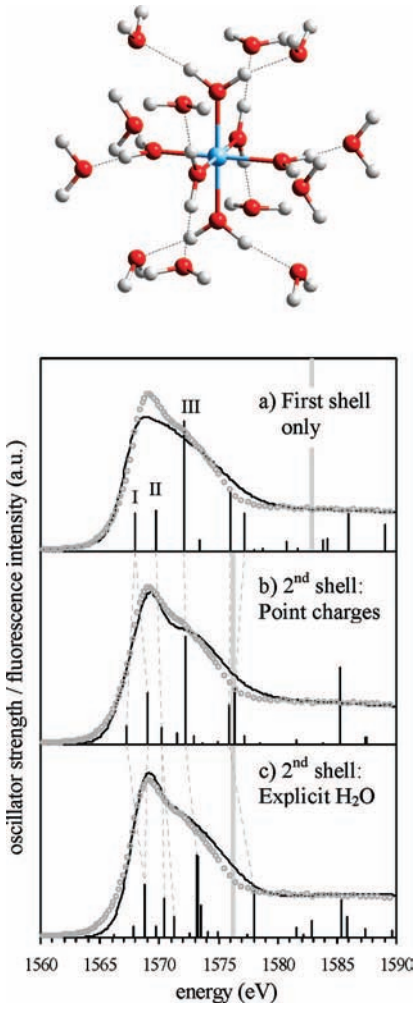

Figure 5. XANES transitions (thin vertical bars), ionization potentials (gray bars), and synthetic spectrum (solid curves) calculated for $Al(H_2O)_6^{3+}$ structures in the presence and absence of second-shell solvation waters, plotted against the 20 mM aqueous $AlCl_3$ spectrum (circles). (a) First-shell waters only (same as Figure 2). (b) Twelve point charge solvation waters. (c) Twelve explicitly defined (electron-bearing) solvation waters. For the calculation in (c), the DZVP basis set was used on O and H. Calculation results have been shifted +4.6−4.7 eV to achieve overlap with experiment. Dashed lines in the plot are used to connect similar transitions in different structures, highlighting the transitions that become split. The schematic shows the placement of the solvation waters.

on equatorial water ligands, though there is still strictly only one set of Al 3p−O 2s bonding orbitals (analogous to orbitals 13−15 in Table 1). The slightly asymmetric shape of the O 2s nodes in the lower energy transition may be indicative of some O 2s/p rehybridization (Figure S2, Supporting Information), giving them the more traditional appearance of the water $4a_1$ orbital.

Addition of the solvation waters as explicit molecules allowed electron sharing between waters in the first and second shells. In this case (Figure 5c), no splitting of transition I is observed, but the intensity of transition I increases relative to transition III. Two contributions analogous to transition II are present in this case. However, the weaker of the two, as well as the other low intensity transitions that have appeared in the near-edge region, exhibit a relatively large amount of electron density on the second-shell waters (Figure S3, Supporting Information), suggesting that these transitions would be weak contributors to the spectrum, if not artifactual. Taken together, the second-shell water results suggest that solvation of the $Al(H_2O)_6^{3+}$ complex may cause some of the splitting responsible for the observed broadness of the XANES spectrum, in addition to the effects discussed above. In both solvation water calculations (Figure 5b,c) the intensity of transition I is enhanced relative to II, making it easier to simulate the spectrum by the Gaussian fitting procedure. Additionally, the ionization potential in the solvation water calculations decreases to ~1576 eV, closer to the expected value in the edge region.

Ab initio geometry optimization calculations have previously been performed on the $Al(H_2O)_6^{3+}\cdot(H_2O)_{12}$ cluster,[16,23,25] demonstrating that the T_h symmetric structure assumed for the second-shell solvated complex in this study is not the minimum energy geometry. This is apparently because none of the protons in the T_h structure are involved in H-bond donation. Geometries that allow H-bond formation between water molecules in the second shell are energetically more favorable. In particular, two geometries were obtained in these studies that constitute local energy equilibria, including one with T symmetry[16,23,25] and a slightly lower energy structure with nearly S_6 symmetry.[16,25] To investigate the effects of symmetry and second-shell H-bonding, StoBe calculations were performed on two additional structures; one with S_6 symmetry, similar to the T_h structure described above in which second-shell waters were oriented with protons outward in a non-H-bonding geometry, and one with nearly S_6 symmetry in which the second-shell waters were rotated inward similar to the reported energy-optimized H-bonding configuration.[25] The results of these calculations are described in detail in the Supporting Information. Though some differences are observed between calculations with different second-shell geometries, the overall effects are similar, including some splitting of transitions I and III, and an enhanced O 2s contribution in structures with solvation waters.

Recently, Matsuo et al. also modeled the XANES spectrum of the aqueous $Al(H_2O)_6^{3+}$ complex using the discrete variational Xα (DV-Xα) method.[43,44] Two geometries were considered in their calculations to investigate the effects of symmetry. The first was for an octahedral geometry with Al−O bond lengths of 1.88 Å, O_h symmetry with respect to Al and O, and water ligands tilted 0° as in the T_h complex above but with an apparently random twist angle.[44] The second was for an asymmetric geometry with six different Al−O bond lengths varying between 1.80 and 2.03 Å, presumably based on the crystal structure of solid $[Al(H_2O)_6](NO_3)_3\cdot 3H_2O$ reported by Herpin and Sudarsanan.[66] The authors observed separate O 2s and 2p contributions in the near-edge region for both geometries. However, though multiple peaks were found distributed throughout the XANES region for the asymmetric complex, only two distinct sets of transitions spaced ~5 eV apart were observed for the O_h complex. Believing that these two transitions would yield features too narrow and distinct in energy to reproduce the experimental spectrum, the authors hypothesized that the equilibrium structure of the aqueous complex is asymmetric, similar to its structure in the nitrate salt. Our results, in contrast, do not suggest that asymmetry of the complex is a necessary assumption in reproducing the XANES spectrum. Though splitting does occur with distortion, the broadness of the spectrum may be explained by split Al 3p−O 2p transitions found to be present in a highly symmetric complex. Band splitting was also observed in our work when water ligands were rotated along the Al−O axes and when solvation waters were added to the structure, suggesting that these effects could also contribute to spectral broadening for a complex exhibiting octahedral symmetry with respect to the O atoms.

Summary

X-ray absorption spectra were collected on dilute aqueous Al solutions in a new soft X-ray endstation to study the coordination geometry and electronic structure of the $Al(H_2O)_6^{3+}$ complex. For interpretation of the spectrum, XANES transitions and synthetic spectra were calculated using the DFT-based software package StoBe. Calculations performed on a highly symmetric (T_h) structure exhibit one Al 3p−O 2s (transition I) and approximately four Al 3p−O 2p (transitions II−V) antibonding orbital contributions. The first two Al 3p−O 2p contributions (II and III), which could be paired with specific bonding orbitals and were assumed to be the more important in the near-edge region, appear to be split due to a weak but significant π-interaction of the Al 3p orbital with the off-axis water ligands. These transitions are retained in calculations that tested nonuniform Al−O bond lengths, reorientation of water ligands (30° inward tilt + random rotation about the Al−O bond axis), and addition of second-shell solvation waters, though further splitting of the transitions was observed. Collectively, these effects are likely responsible for the observed broadness of the XANES spectrum for this complex. Addition of the solvation shell also enhanced the oscillator strength of the low-energy O 2s contribution, bringing the synthetic spectrum into closer agreement with experiment. These results therefore demonstrate that, although geometric distortions are possible, the XANES spectrum is consistent with an octahedrally symmetric complex, as proposed on the basis of ab initio geometry optimizations. This work illustrates the utility of the XANES spectroscopy technique in understanding the bonding environment of aqueous Al complexes and demonstrates the validity of the StoBe calculations in modeling Al-edge XANES transitions. Work currently in progress includes comparative studies of Al-aqua/hydroxo and other organic and inorganic ligand complexes.

Acknowledgment. This project was supported by grants from NSF (Chemical Sciences-EMSI program) and from the BES, DOE (Geosciences). M.B.H. also acknowledges financial support from the EPA STAR and NSF graduate research fellowships. The Advanced Light Source is supported by the Director, Office of Science, Office of Basic Energy Sciences, of the U.S. Department of Energy under Contract No. DE-AC02-05CH11231. We thank Tolek Tyliszczak, Hendrik Bluhm, Mary Gilles, and David Shuh at Beamline 11.0.2, Advanced Light Source, for assistance with experimental design and setup. We also thank Kate Campbell and two anonymous reviewers for helpful comments on the manuscript.

Supporting Information Available: Energies and electron isodensity plots of the occupied molecular orbitals of the T_h-symmetric $Al(H_2O)_6^{3+}$ complex, isodensity plots of the antibonding orbitals involved in XANES transitions for the T_h-symmetric $Al(H_2O)_6^{3+}\cdot(H_2O)_{12}$ structures, and results of the S_6-symmetric $Al(H_2O)_6^{3+}$ and $Al(H_2O)_6^{3+}\cdot(H_2O)_{12}$ calculations. This information is available free of charge via the Internet at http://pubs.acs.org.

References and Notes

(1) Foy, C. D.; Chaney, R. L.; White, M. C. *Annu. Rev. Plant Phys. Plant Mol. Biol.* **1978**, *29*, 511.

(2) Kochian, L. V. *Annu. Rev. Plant Phys. Plant Mol. Biol.* **1995**, *46*, 237.

(3) Burrows, W. D.; Hem, J. D. *Crit. Rev. Environ. Control.* **1977**, *7*, 167.

(4) Gensemer, R. W.; Playle, R. C. *Crit. Rev. Environ. Sci. Technol.* **1999**, *29*, 315.

(5) Kerr, D. N. S.; Ward, M. K.; Ellis, H. A.; Simpson, W.; Parkinson, I. S. Aluminum intoxication in renal disease. In *Aluminum in Biology and Medicine*; Ciba Foundation Symposium 169; John Wiley & Sons: Chichester, U.K., 1992.

(6) Good, P. F.; Perl, D. P. *Neurobiol. Aging* **1994**, *15*, S28.

(7) Perl, D. P.; Gajdusek, D. C.; Garruto, R. M.; Yanagihara, R. T.; Gibbs, C. J. *Science* **1982**, *217*, 1053.

(8) Gauthier, E.; Fortier, I.; Courchesne, F.; Pepin, P.; Mortimer, J.; Gauvreau, D. *Environ. Res.* **2000**, *84*, 232.

(9) Gupta, V. B.; Anitha, S.; Hegde, M. L.; Zecca, L.; Garruto, R. M.; Ravid, R.; Shankar, S. K.; Stein, R.; Shanmugavelu, P.; Rao, K. S. J. *Cell. Mol. Life Sci.* **2005**, *62*, 143.

(10) Sullivan, P. J.; Yelton, J. L.; Reddy, K. J. *Environ. Geol. Water Sci.* **1988**, *11*, 283.

(11) Lawrence, G. B.; Driscoll, C. T. *Environ. Sci. Technol.* **1988**, *22*, 1293.

(12) Berthon, G. *Coord. Chem. Rev.* **2002**, *228*, 319.

(13) Kinraide, T. B. *J. Exp. Bot.* **1997**, *48*, 1115.

(14) Amira, S.; Spangberg, D.; Hermansson, K. *J. Chem. Phys.* **2006**, *124*, 104501.

(15) Bakker, A.; Hermansson, K.; Lindgren, J.; Probst, M. M.; Bopp, P. A. *Int. J. Quantum Chem.* **1999**, *75*, 659.

(16) Bock, C. W.; Markham, G. D.; Katz, A. K.; Glusker, J. P. *Inorg. Chem.* **2003**, *42*, 1538.

(17) Bylaska, E. J.; Valiev, M.; Rustad, J. R.; Weare, J. H. *J. Chem. Phys.* **2007**, *126*, 1.

(18) Ikeda, T.; Hirata, M.; Kimura, T. *J. Chem. Phys.* **2003**, *119*, 12386.

(19) Kowall, T.; Caravan, P.; Bourgeois, H.; Helm, L.; Rotzinger, F. P.; Merbach, A. E. *J. Am. Chem. Soc.* **1998**, *120*, 6569.

(20) Kubicki, J. D. *J. Phys. Chem. A* **2001**, *105*, 8756.

(21) Lubin, M. I.; Bylaska, E. J.; Weare, J. H. *Chem. Phys. Lett.* **2000**, *322*, 447.

(22) Martinez, J. M.; Pappalardo, R. R.; Marcos, E. S. *J. Am. Chem. Soc.* **1999**, *121*, 3175.

(23) Rudolph, W. W.; Mason, R.; Pye, C. C. *Phys. Chem. Chem. Phys.* **2000**, *2*, 5030.

(24) Wasserman, E.; Rustad, J. R.; Xantheas, S. S. *J. Chem. Phys.* **1997**, *106*, 9769.

(25) Bock, C. W.; Markham, G. D.; Katz, A. K.; Glusker, J. P. *Theor. Chem. Acc.* **2006**, *115*, 100.

(26) Connick, R. E.; Poulson, R. E. *J. Am. Chem. Soc.* **1957**, *79*, 5153.

(27) Connick, R. E.; Fiat, D. N. *J. Chem. Phys.* **1963**, *39*, 1349.

(28) Bol, W.; Welzen, T. *Chem. Phys. Lett.* **1977**, *49*, 189.

(29) Caminiti, R.; Licheri, G.; Piccaluga, G.; Pinna, G.; Radnai, T. *J. Chem. Phys.* **1979**, *71*, 2473.

(30) Bugaev, L. A.; Ildefonse, P.; Flank, A. M.; Sokolenko, A. P.; Dmitrienko, H. V. *J. Phys.: Condens. Matter* **1998**, *10*, 5463.

(31) Cabaret, D.; Sainctavit, P.; Ildefonse, P.; Flank, A. M. *J. Phys.: Condens. Matter* **1996**, *8*, 3691.

(32) Chaplais, G.; Prouzet, E.; Flank, A. M.; Le Bideau, J. *New J. Chem.* **2001**, *25*, 1365.

(33) Doyle, C. S.; Traina, S. J.; Ruppert, H.; Kendelewicz, T.; Rehr, J. J.; Brown, G. E. *J. Synchrotron Rad.* **1999**, *6*, 621.

(34) Froba, M.; Wong, J.; Rowen, M.; Brown, G. E.; Tanaka, T.; Rek, Z. *Physica B* **1995**, *209*, 555.

(35) Giuli, G.; Pratesi, G.; Corazza, M.; Cipriani, C. *Am. Mineral.* **2000**, *85*, 1172.

(36) Ildefonse, P.; Kirkpatrick, R. J.; Montez, B.; Calas, G.; Flank, A. M.; Lagarde, P. *Clays Clay Miner.* **1994**, *42*, 276.

(37) Ildefonse, P.; Calas, G.; Flank, A. M.; Lagarde, P. *Nucl. Instrum. Methods Phys. Res., Sect. B* **1995**, *97*, 172.

(38) Ildefonse, P.; Cabaret, D.; Sainctavit, P.; Calas, G.; Flank, A. M.; Lagarde, P. *Phys. Chem. Miner.* **1998**, *25*, 112.

(39) van Bokhoven, J. A.; Sambe, H.; Ramaker, D. E.; Koningsberger, D. C. *J. Phys. Chem. B* **1999**, *103*, 7557.

(40) van Bokhoven, J. A.; Nabi, T.; Sambe, H.; Ramaker, D. E.; Koningsberger, D. C. *J. Phys.: Condens. Matter* **2001**, *13*, 10247.

(41) Wu, Z. Y.; Marcelli, A.; Mottana, A.; Giuli, G.; Paris, E.; Seifert, F. *Phys. Rev. B* **1996**, *54*, 2976.

(42) Yoon, T. H.; Johnson, S. B.; Benzerara, K.; Doyle, C. S.; Tyliszczak, T.; Shuh, D. K.; Brown, G. E. *Langmuir* **2004**, *20*, 10361.

(43) Matsuo, S.; Wakita, H. *Struct. Chem.* **2003**, *14*, 69.

(44) Matsuo, S.; Shirozu, K.; Tateishi, Y.; Wakita, H. *Adv. Quantum Chem.* **2003**, *42*, 407.

(45) Hay, M. B. Advances in the Molecular-Scale Understanding of Geochemical Processes: Carboxyl Structures in Natural Organic Matter, Organosulfur Cycling in Soils, and the Coordination Chemistry of Aqueous Aluminum. PhD. dissertation, Princeton University, 2007.

(46) Ressler, T. *J. Synchrotron Rad.* **1998**, *5*, 118.

(47) Hermann, K.; Pettersson, L. G. M.; Casida, M. E.; Daul, C.; Goursot, A.; Koester, A.; Proynov, E.; St-Amant, A.; Salahub, D. R.; Carravetta, V.; Duarte, H.; Godbout, N.; Guan, J.; Jamorski, C.; Leboeuf,

M.; Malkin, V.; Malkina, O.; Nyberg, M.; Pedocchi, L.; Sim, F.; Triguero, L.; Vela, A. *StoBe-deMon version 1.0; StoBe Software*; 2002.

(48) Becke, A. D. *Phys. Rev. A* **1988**, *38*, 3098.

(49) Perdew, J. P. *Phys. Rev. B* **1986**, *34*, 7406.

(50) Triguero, L.; Pettersson, L. G. M.; Agren, H. *Phys. Rev. B* **1998**, *58*, 8097.

(51) Slater, J. C.; Johnson, K. H. *Phys. Rev. B* **1972**, *5*, 844.

(52) Nilsson, A.; Ogasawara, H.; Cavalleri, M.; Nordlund, D.; Nyberg, M.; Wernet, P.; Pettersson, L. G. M. *J. Chem. Phys.* **2005**, *122*.

(53) Cavalleri, M.; Naslund, L. A.; Edwards, D. C.; Wernet, P.; Ogasawara, H.; Myneni, S.; Ojamae, L.; Odelius, M.; Nilsson, A.; Pettersson, L. G. M. *J. Chem. Phys.* **2006**, *124*.

(54) Schaftenaar, G.; Noordik, J. H. *J. Comput. Aided Mol. Des.* **2000**, *14*, 123.

(55) Triguero, L.; Plashkevych, O.; Pettersson, L. G. M.; Agren, H. *J. Electron Spectrosc.* **1999**, *104*, 195.

(56) Kutzelnigg, W.; Fleischer, U.; Schindler, M. IGLO-method: Ab-initio calculation and interpretation of NMR chemical shifts and magnetic susceptibilities. In *The NMR Basic Principles and Progress*; Diehl, P., Ed.; Springer: New York, 1990; *Vol. 23*.

(57) Edwards, D. C.; Myneni, S. C. B. *J. Phys. Chem. A* **2006**, *110*, 11809.

(58) Godbout, N.; Salahub, D. R.; Andzelm, J.; Wimmer, E. *Can. J. Chem.* **1992**, *70*, 560.

(59) Guan, J.; Duffy, P.; Carter, J. T.; Chong, D. P.; Casida, K. C.; Casida, M. E.; Wrinn, M. *J. Chem. Phys.* **1993**, *98*, 4753.

(60) Lie, G. C.; Clementi, E. *J. Chem. Phys.* **1973**, *60*, 1275.

(61) Martell, A. E.; Smith. R. M. *Database 46: NIST Critically Selected Stability Constants of Metal Complexes*, Version 7 [Electronic Resource]; NIST Standard Reference Data; NIST: Gaithersburg, MD, 1995.

(62) Broadbent, R. D.; Neilson, G. W.; Sandstrom, M. *J. Phys.: Condens. Matter* **1992**, *4*, 639.

(63) Guo, J. H.; Luo, Y.; Augustsson, A.; Rubensson, J. E.; Sathe, C.; Agren, H.; Siegbahn, H.; Nordgren, J. *Phys. Rev. Lett.* **2002**, *89*, 137402.

(64) Cotton, F. A.; Daniels, L. M.; Murillo, C. A.; Quesada, J. F. *Inorg. Chem.* **1993**, *32*, 4861.

(65) Fulton, R. L.; Perhacs, P. *J. Phys. Chem. A* **1998**, *102*, 8988.

(66) (a) Herpin, P.; Sudarsanan, K. *Bull. Soc. Franç. Minér.Crist.* **1965**, *88*, 595. (b) Note, however, that the crystal structure of this compound has since been restudied; see: Lazar, D.; Ribár, B.; Prelesnik, B. *Acta Crystallogr.* **1991**, *C47*, 2282. In the more recent work, the geometry of the $Al(H_2O)_6$ complex within the crystal was determined to be more symmetric than previously thought.

JP802675V